Coupling metal–organic frameworks and g-C$_3$N$_4$ to derive Fe@N-doped graphene-like carbon for peroxymonosulfate activation: Upgrading framework stability and performance

Chao Liu[a], Liyuan Liu[a], Xing Tian[a], Yiping Wang[a], Ruoyu Li[a], Yuting Zhang[a], Zilong Song[a], Bingbing Xu[b], Wei Chu[c], Fei Qi[a,*], Amir Ikhlaq[d]

[a] *Beijing Key Lab for Source Control Technology of Water Pollution, College of Environmental Science and Engineering, Beijing Forestry University, Beijing 100083, China*
[b] *State Key Lab of Environmental Criteria and Risk Assessment, Chinese Research Academy of Environmental Sciences, Beijing 100012, China*
[c] *Department of Civil and Environmental Engineering, The Hong Kong Polytechnic University, Hung Hom, Kowloon, Hong Kong*
[d] *Institute of Environment Engineering and Research, University of Engineering and Technology, GT Road, 54890, Lahore, Punjab, Pakistan*

ARTICLE INFO

ABSTRACT

A highly active mediator (Fe@N-doped graphene-like carbon) for peroxymonosulfate (PMS) activation was prepared by employing g-C$_3$N$_4$ assisting NH$_2$-MIL-53(Fe) as the precursor. The addition of combined nitrogen sources (g-C$_3$N$_4$ and NH$_2$ groups) not only stabilized the phase composition and framework morphology, but also improved PMS activation performance significantly. In addition, the introduction of g-C$_3$N$_4$ increased the surface area. Electron paramagnetic resonance (EPR) spectroscopy and radical quenching experiments identified singlet oxygen (^{1}O$_2$), superoxide radicals (O$_2$$^{\bullet-}$), hydroxyl radicals (•OH), and sulfate radicals (SO$_4$$^{\bullet-}$) as the reactive oxygen species (ROS) in 4-aminobenzoic acid ethyl ether (ABEE) degradation *via* a combination process of nonradical and radical processes. The variable chemical valences of iron nanoparticles and quaternary-N, pyrrolic-N, pyridinic-N, and carbonyl (C=O) groups in the support contributed to the outstanding catalytic activity. A possible mechanism for PMS activation by Fe@N-doped graphene-like carbon for ABEE degradation was proposed, which involved sp^2 hybridized carbon and electron-rich sp^2 sites of the graphitic domain activating PMS *via* electron transfer. Intermediates were identified using liquid chromatography-quadrupole time-of-flight mass spectrometry (LC-Q-TOF-MS). The degradation pathway of ABEE was reported for the first time in the advanced oxidation process field. Based on intermediate identification of sulfamethoxazole (SMX) degradation, six intermediates were first reported and a new reaction pathway established. This work provides a promising approach to the rational design of high-performance active mediators for environmental remediation.

1. Introduction

Water pollution caused by recalcitrant pollutants, such as pharmaceuticals and endocrine disruptors, is an increasing problem owing to the adverse effects these substances showed on human health and aquatic ecosystems [1]. Therefore, various water purification technologies have been applied to remove pharmaceuticals from the environment, such as adsorption, biological degradation, oxidation, and membrane filtration [2]. Among these, sulfate radical-based advanced oxidation processes (SR-AOPs) have proven to be promising and

efficient technologies [3]. Compared with traditional hydroxyl radical (•OH)-based AOPs, SR-AOPs have shown more efficient performance in recalcitrant pollutant degradation owing to their higher oxidative potentials (2.5–3.1 V) [4], wide pH range (2–9), longer half-life period (30–40 μs) [5], and reaction selectivity [6]. Most commonly, SO$_4$$^{\bullet-}$ generation can be achieved through peroxymonosulfate (PMS) or peroxydisulfate (PS) activation using various approaches, such as UV [7], heat [8], base [9], transition metals [10], and solid catalysts including metal oxides, carbon materials [11] and metallic glasses [12–14]. Heterogeneous solid mediators have also been widely applied as highly

effective PMS activators [15] and are preferred because they avoid to the additional costs.

Recent studies showed that doping nitrogen atoms into carbon matrixes can greatly improve their catalytic performance towards PMS activation [16]. Doped nitrogen not only increases the surface basicity for PMS adsorption, but also facilitates electron transfer with PMS by activating neighboring sp^2 carbon atoms [17]. In particular, nitrogen-doped porous carbon obtained from the thermal treatment of a parent metal–organic framework (MOF) template has been shown to be an efficient PMS activator for reactive oxygen species (ROS) formation [18,19]. MOF-derived carbon materials also have distinct advantages for PMS activation, such as hierarchical porous structures, large surface areas, and abundant active sites [20]. Fe-based nanoparticles (Fe/Fe$_3$C NPs) synthesized by simple pyrolysis of NH$_2$-MIL-88B exhibited efficient performance in 4-chlorophenol degradation through PMS activation [21]. Nitrogen-doped graphene synthesized by the one-step pyrolysis of mixed MIL-100(Fe)/dicyandiamide exhibited high catalytic activities for phenol degradation through PMS activation [22]. Lin et al. constructed porous Co/carbon nanocomposites from the thermal decomposition of ZIF-67 under nitrogen atmosphere to active Oxone for caffeine degradation [23]. Li et al. fabricated graphene-encapsulated Fe$_x$Co$_y$ nanocages derived from Prussian blue analogue as efficient PMS activators [24]. Unfortunately, MOF-derived carbon materials tend to undergo serious particle aggregation and framework collapse during MOF pyrolysis. Significantly, active metal ions leaching from MOF-derived carbon materials was found [21,24], which declined the performance on PMS activation and resulted in the toxic metal ions occurrence. However, this vital issue was ignored widely for MOF-derived carbon materials, even was concealed.

G-C$_3$N$_4$ has been reported as an excellent support template that plays a vital role in preventing MOFs aggregating during pyrolysis [25,26]. Therefore, in this study, g-C$_3$N$_4$ was selected as both the template precursor and nitrogen source to develop MOF-derived nitrogen carbon materials with improved properties and PMS activation performance for the degradation of refractory micro-organic contaminants in aqueous media. Herein, g-C$_3$N$_4$ provided an additional external nitrogen source and improved the stability and specific surface area of pyrolysis products derived from MOF morphologies/structures. This development resulting from adding an external nitrogen source (g-C$_3$N$_4$) will elevate the performance of PMS activation and eliminate the active metal ions leaching to prolong the using life and avoid the toxic metal ions secondary exposure.

Based above, the effect of adding g-C$_3$N$_4$ on the crystal phase, surface morphology, and performance of the obtained Fe@N-doped graphene-like carbon for PMS activation were investigated in detail. Additionally, the synergistic effect of iron, nitrogen and graphene-like carbon in the obtained Fe@N-doped graphene-like carbon was studied using model probes (4-aminobenzoic acid ethyl ester (ABEE) and sulfamethoxazole (SMX)) to determine the degradation efficiency and identify the ROS involved. Finally, the surface-active sites and reaction mechanisms of Fe@N-doped graphene-like carbon for PMS activation were proposed. In this study, the novelty point was the synthesis of a novel Fe@N-doped graphene-like carbon and the interface reaction mechanism of its activating PMS for refractory drugs degradation. This novel efficient activator exhibited great potential as a SR-AOP catalyst for applications to hazardous contaminant remediation in water.

2. Materials and methods

2.1. Chemicals

Oxone (2KHSO$_5$·KHSO$_4$·K$_2$SO$_4$) and 2-aminoterephthalic acid (NH$_2$-BDC) were purchased from Alfa Aesar Chemicals Co., Ltd. (Shanghai, China). Iron (III) chloride hexahydrate (FeCl$_3$·6H$_2$O) and terephthalic acid (H$_2$BDC) were supplied by Xiya Chemical Reagent Co., Ltd. (Shandong, China). Urea, N,N-dimethylformamide (DMF), ethanol, and

tert-butanol were obtained from Beijing Chemical Works (Beijing, China). Sulfamethoxazole (SMX) was obtained from J&K China Chemical Ltd. (Beijing, China). 4-Aminobenzoic acid ethyl ester (ABEE), 5,5-dimethyl-1-pyrroline N-oxide (DMPO), and 2,2,6,6-teramethylpiperidine (TEMP) were obtained from TCI Development Co., Ltd. (Shanghai, China). High-performance liquid chromatography (HPLC)-grade methanol was purchased from Sigma-Aldrich (Shanghai, China). Deionized water was obtained using a Milli-Q water purification system and used in all experiments. Chemicals used in this study were all commercially available and used directly without purification.

2.2. Synthesis of Fe@N-doped graphite-like carbon

G-C$_3$N$_4$ was prepared according to a previous report [27], with a typical synthetic procedure provided in Text S1 (Supporting Information, SI). FeCl$_3$·6H$_2$O (0.674 g) and NH$_2$-BDC (0.4525 g) were dissolved in DMF (56 mL). A certain amount of g-C$_3$N$_4$ was then added to this homogeneous solution and treated with ultrasound (30 kHz, 500 W) for 0.5 h. The mixed solution was then transferred into a Teflon-lined stainless-steel autoclave, sealed, and heated at 170°C for 24 h. The resulting powder was centrifuged at 8,000 rpm for 5 min and washed several times with DMF and EtOH, respectively, to remove solvent. The obtained product, NH$_2$-MIL-53(Fe)/g-C$_3$N$_4$, was dried under vacuum at 100°C for 10 h and then placed in a tube furnace, heated to 650°C at a heating rate of 5 °C/min under flowing nitrogen (100 mL/min), and held at that temperature for 3 h. After cooling to room temperature, the resulting black powder was collected. The influence of ligand structures and g-C$_3$N$_4$ dosage was investigated to optimize preparation conditions, as described in detail in Text S2. The synthesis conditions and definitions of the corresponding samples are shown in Table S1.

2.3. Characterization of Fe@N-doped graphene-like carbon

The crystal structure of the obtained sample was characterized using powder X-ray diffraction (XRD) on a Shimadzu XRD-7000 diffractometer (Japan) using Cu Kα radiation (λ = 1.5418 Å). The morphology of the as-prepared samples was characterized using field emission scanning electron microscopy (FE-SEM, Merlin, Germany) and high-resolution transmission electron microscopy (HR-TEM, JEOL-2010 F, Japan). The composition and surface chemical states were identified by X-ray photoelectron spectroscopy (XPS; AXIS Ultra, Kratos Analytical Ltd., Japan). The Brunauer-Emmett-Teller (BET) specific surface area was measured from the N$_2$ adsorption/desorption isotherm using a Builder SSA-7000 surface area and pore size analyzer (Beijing Builder Electronic Technology CO., LTD, China).

2.4. Performance evaluation of PMS activation for refractory drug degradation

ABEE, found in sunscreen and many over-the-counter anesthetic ointments [28], was selected as the degradation probe to test PMS activation performance of Fe@N-doped graphene-like carbon. To study the selectivity of as-obtained Fe@N-doped graphene-like carbon for the degradation of micro-organic contaminants, SMX, a commonly used sulfonamide antibiotic, was chosen as the target probe [29]. The reaction procedure for organics degradation by PMS activation in aqueous solution and corresponding analysis methods are described in Text S3.

3. Results and discussion

3.1. Confirmation of nitrogen source in precursor of Fe@N-doped graphene-like carbon

Different nitrogen sources (NH$_2$-BDC as internal source, g-C$_3$N$_4$ as external source, and their combination) were used to fabricate Fe@N-
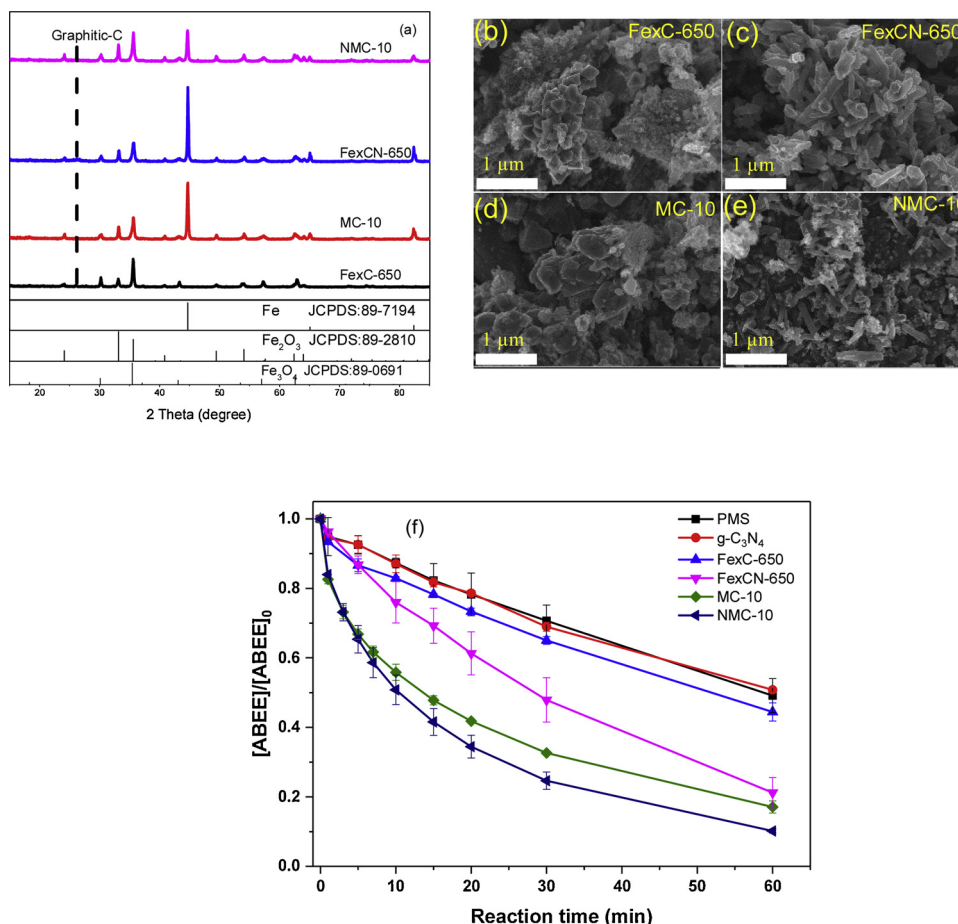
Fig. 1. (a) XRD patterns of FexC-650, FexCN-650, MC-10, NMC-10; SEM images of (b) FexC-650, (c) MC-10, (d) FexCN-650, (e) NMC-10; Removal efficiency of ABEE in different reaction within 60 min (f).
Reaction conditions: [ABEE] = 0.06 mM, [PMS] = 0.65 mM, [Catalyst] = 50 mg/L, initial pH = 7.0.

doped graphene-like carbon in this study to obtain an efficient nitrogen structure. As shown in Fig. 1(a), the peak at 26.1° corresponding to (002) plane of graphitic carbon is observed, providing a supportive evidence for the presence of particular graphitic structures. The introduction of a nitrogen source promoted Fe^0 formation in FexCN-650 and MC-10, because added nitrogen reduced the iron oxides to form Fe^0. However, the addition of g-C_3N_4 as an external (MC-10) or combined (NMC-10) nitrogen source decreased the diffraction intensity of Fe^0, which might be due to the increase in thickness of the carbon layer encapsulation [30].

Without adding any nitrogen source, the polyhedral shape of MIL-53(Fe) collapsed significantly after pyrolysis (Fig. 1(b)). The addition of an internal nitrogen source (NH$_2$-MIL-53(Fe)) only slightly improved the stability to avoid collapse, while the aggregation was still clearly observed (Fig. 1(c)). The addition of g-C_3N_4 effectively prevented the aggregation of pyrolysis products and significantly improved the dispersion of nanoparticles (Fig. 1(d)), such as in MC-10. This was more obvious when the combined nitrogen source was used (such as NMC-10 in Fig. 1(e)). After g-C_3N_4 addition, the uniform polyhedral shapes of MC-10 and NMC-10 were significantly maintained.

PMS activation performance of as-obtained Fe@N-doped graphene-like carbon was evaluated using ABEE as probe (Fig. 1(f)). PMS alone degraded 40% ABEE in 60 min, indicating that PMS self-decomposition was able to oxidize ABEE at pH 7.0. A similar result has been reported previously [31]. Herein, g-C_3N_4 did not contribute to enhancing ABEE degradation performance, which was consistent with other results [32,33]. Around 56% and 79% of ABEE was degraded by PMS activation using FexC-650 and FexCN-650, respectively. This confirmed that

Fe@N-doped graphene-like carbon showed good activity for PMS activation and micro-contaminant degradation. NMC-10, obtained by combining g-C_3N_4 and NH$_2$ groups in the precursors, showed outstanding PMS activation performance. Herein, although MC-10 and NMC-10 showed similar phase compositions, the nitrogen content of NMC-10 was higher than that of MC-10. Accordingly, the increasing nitrogen content in Fe@N-doped graphene-like carbon was expected to show a positive effect on PMS activation performance. More importantly, the introduction of nitrogen into the structure of Fe@N-doped graphene-like carbon not only improved the framework stability, but also significantly improved the PMS activation performance. Therefore, the addition of combined nitrogen sources (g-C_3N_4 and NH$_2$ groups) to the precursors was selected for further study.

3.2. Effect of g-C_3N_4 content on phase, morphology, and performance

The crystal structure of NMC-X, where X represents g-C_3N_4 content (10, 15, 20, 50, or 70 wt%) was characterized, as shown in Fig. 2(a). These structures exhibited similar XRD features, with a weak signal at approximately 26° corresponding to (002) facets of graphitic carbon with a low degree of graphitization [34]. When g-C_3N_4 content increased to 50 wt%, the corresponding α-Fe_2O_3 peak disappeared, implying that introducing g-C_3N_4 was beneficial for the formation of more stable phases. Second, the diffraction peaks became gradually weaker with increasing g-C_3N_4 content, which might be due to thickening of the carbon layer of Fe@N-doped graphene-like carbon on the metal particle surface [30].

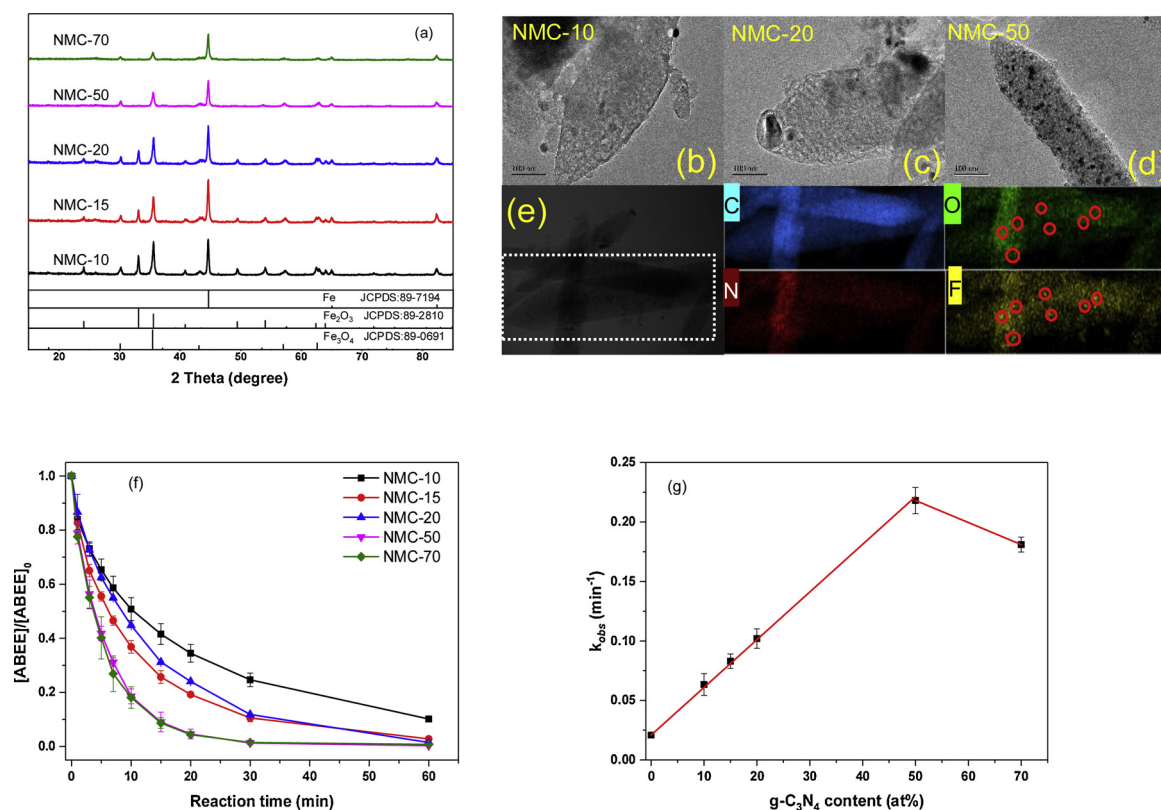The SEM images in Fig. S1 showed that the pyrolysis products

Fig. 2. (a) XRD patterns of NMC-10, NMC-15, NMC-20, NMC-50, NMC-70. HR-TEM images of (b) NMC-10, (c) NMC-20, (d) NMC-50; Selected-area scanning TEM and elemental mapping images of C, O, N and Fe (e); Removal efficiency of ABEE under different conditions (f).
Reaction conditions: [ABEE] = 0.06 mM, [PMS] = 0.65 mM, [Catalyst] = 50 mg/L, initial solution pH = 7.0. Effect of g-C_3N_4 content on the degradation efficiency of ABEE (g).

roughly maintained their original spindle shape. The particle shape became more complete and the dispersion increasingly uniform with the increasing of g-C_3N_4 content. However, the carbon layer accumulation was also becoming more and more serious. NMC-X morphology was further studied using HR-TEM (Figs. 2(b)–(d)). With increasing g-C_3N_4 content, the spindle framework of NMC-10 collapsed, but the framework was well-retained, with more metal nanoparticles appearing inside the framework. The elemental mapping images of NMC-20, as shown in Fig. 2(e), confirmed that carbon, oxygen, nitrogen, and iron elements were homogeneously distributed over the selected area, indicating that iron and nitrogen were co-doped in the carbon architecture. Furthermore, the distributions of iron and oxygen was similar. However, there still some points highlighted in the carbon skeleton in Iron mapping image, but was dark in Oxygen mapping image. This appearance might be duo to the presence of aggregation of Fe. According to the analysis results of XPS spectrums (Fig. S13), it is speculated that this may be caused by Zero Valence Iron (Fe^0) and nano iron oxides. In summary, the pyrolysis of combined g-C_3N_4 and NH$_2$-MIL-53(Fe) confined iron nanoparticles in porous carbon and resulted in a more stable structure. The pore character and surface area of the pyrolysis products were characterized by N$_2$ adsorption-desorption measurements. As shown in Fig. S2, a type-IV isotherm with a pronounced hysteresis loop was observed for the sample of FexCN-650 and NMC-50 indicating the porous structure of the catalyst. The synthesized NMC-50 showed a higher specific surface area of 212.37 m^2/g (Fig. S2(b)) than FexCN-650 (specific surface area, 188.17 m^2/g (Fig. S2(a))). The pore size of FexCN-650 and NMC-50 is mainly centered at about 3.80 nm. This indicates that the introduction of g-C_3N_4 during the pyrolysis process increased the specific surface area, and the additional external nitrogen source was not the crucial factor determining the pore size distributions.

The chemical compositions of NMC-X were shown in Table S2, with increasing g-C_3N_4 content, contents of C and Fe basically remained unchanged. However, N content increased firstly and then decreased, and the highest sample was NMC-50. Accordingly, the C/N ratio was 21.64, 19.35 or 14.26 for NMC-10, NMC-20 or NMC-70, respectively, much higher than that of NMC-50 (C/N = 12.73). The different C/N ratios of NMC-X were likely correlated to the dispersion of g-C_3N_4 on surface.

Figs. 2(f) and (g) show the effect of g-C_3N_4 content on PMS activation for ABEE degradation. As g-C_3N_4 content increased from 10% to 50%, the catalytic activity of Fe@N-doped graphene-like carbon improved gradually, with NMC-50 showing the highest catalytic activity. However, the catalytic activity decreased as the g-C_3N_4 content was further increased from 50% to 70%. This was attributed to g-C_3N_4 phase agglomeration blocking the pores and leading to a decrease in catalytic active sites [35]. This result was also confirmed by SEM (Fig. S1). Based on these results, NMC-50 was selected for further study due to showing the best performance and better stability and iron nanoparticle dispersibility.

3.3. PMS activation performance of NMC-50 for refractory drug degradation

The effects of several reaction parameters on ABEE degradation efficiency, including catalyst loading, PMS dosage, and substrate concentration, were evaluated, as shown in Fig. S3 and Text S4.

The performance of PMS-based SR-AOP was known to be mostly dependent on the initial solution pH [36]. As shown in Fig. 3(a), ABEE was completely degraded within 60 min at pH 3.4–8.0, indicating that NMC-50 showed good performance for PMS activation over a wide solution pH range. The value of k_{obs} decreased gradually as initial
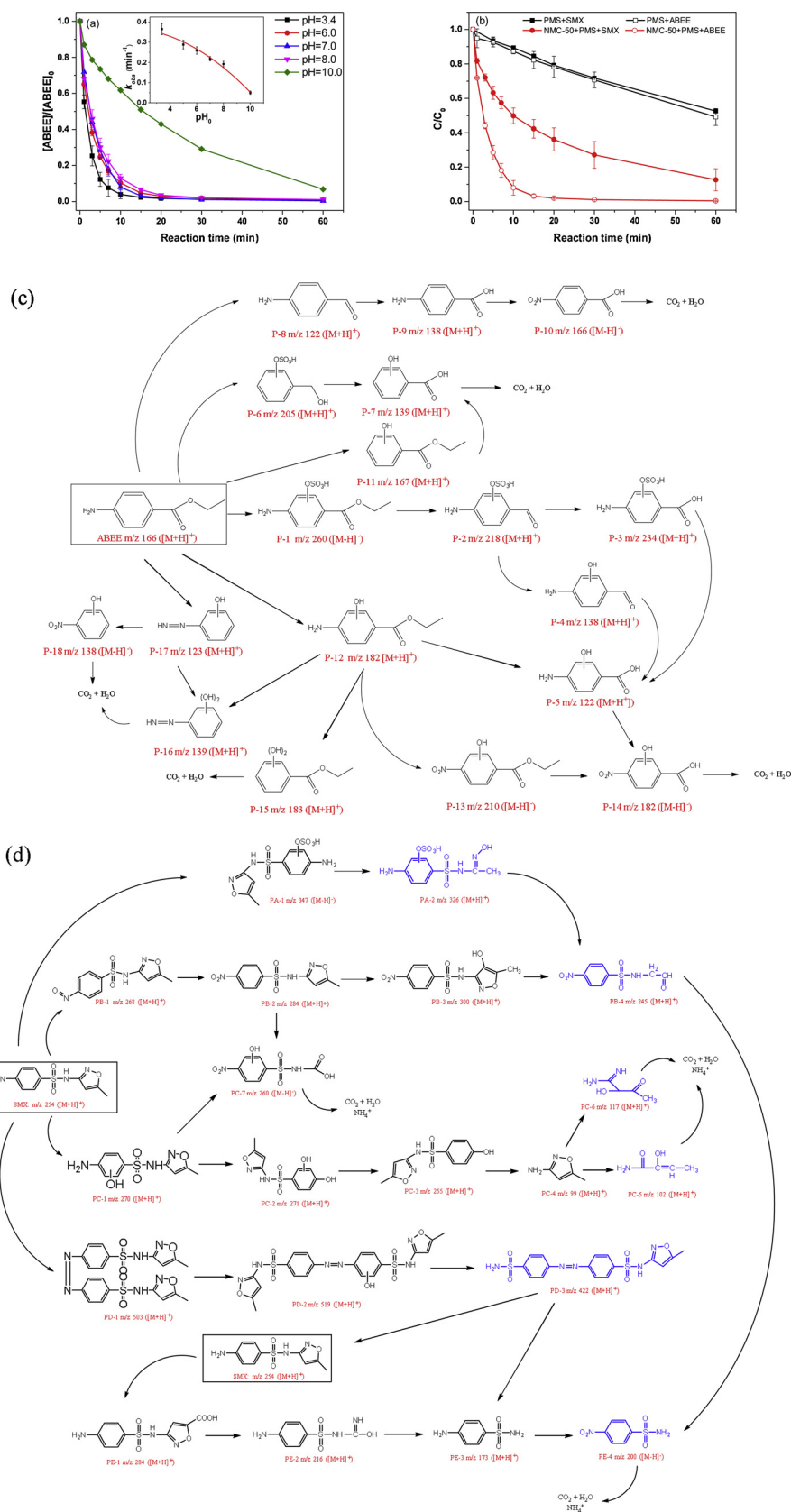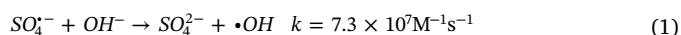
Fig. 3. Effect of pH on the ABEE degradation (a); Removal of ABEE and SMX using NMC-50 activated PMS (b); Propose reaction pathway for ABEE (c) and SMX (d) degradation.
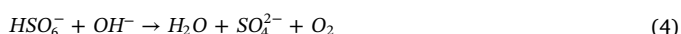
Reaction conditions: [NMC-50] = 50 mg/L, [PMS] = 0.65 mM, [ABEE] = [SMX] = 0.06 mM, initial pH = 7.0.

solution pH increased, which implied that higher pH values were unfavorable for PMS activation by NMC-50. The pKa values of ABEE and PMS have been reported as 2.5 [28] and 9.4 [37], respectively. Therefore, the ionization states of ABEE$^-$ and HSO$_5^-$ did not change over the pH range 3.4–8.0. As no electrostatic attraction was observed between ABEE and PMS in this study, it was not the driving force of this reaction.
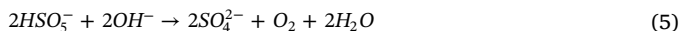
In acidic solution, SO$_4^{\bullet-}$ is the main reactive radical formed from PMS decomposition. As the initial solution pH increased from acidic to basic, more •OH was formed instead of SO$_4^{\bullet-}$, according to Eq. (1) [38].

$$SO_4^{\bullet-} + OH^- \rightarrow SO_4^{2-} + \bullet OH \quad k = 7.3 \times 10^7 M^{-1}s^{-1} \quad (1)$$

Buxton et al. reported that the •OH showed a standard reduction potential of 2.7 V in acidic solution and 1.8 V in neutral solution [39]. In neutral or basic pH solutions, •OH showed a lower redox potential than SO$_4^{\bullet-}$. Considering the transformation of Eq. (1), the oxidation capacity under neutral or basic pH solutions decreased, which led to a decrease in ABEE degradation performance with increasing initial solution pH. Furthermore, the obvious decrease in k_{obs} at pH 10.0 was probably due to the formation of dianion SO$_5^{2-}$ from PMS under basic conditions, which showed weak oxidizing power and was not able to be activated by the catalyst [40], as shown in Eq. (2). SO$_5^{2-}$ would be transformed into HSO$_6^-$ and sulfate (Eqs. (3) and (4)), which also decreased the performance of PMS activation.

$$HSO_5^- \Leftrightarrow SO_5^{2-} + H^+ \quad pKa = 9.4 \quad (2)$$

$$HSO_5^- + SO_5^{2-} \rightarrow HSO_6^- + SO_4^{2-} \quad (3)$$

$$HSO_6^- + OH^- \rightarrow H_2O + SO_4^{2-} + O_2 \quad (4)$$

Furthermore, as another reason for the diminished performance, PMS was prone to decomposition to sulfate and oxygen gas by OH$^-$ (Eq. (5)) [41].

$$2HSO_5^- + 2OH^- \rightarrow 2SO_4^{2-} + O_2 + 2H_2O \quad (5)$$

The variation in the solution pH in ABEE degradation by NMC-50 activation PMS are shown in Fig. S4 and Text S5.

As a widely used sulfonamide antibiotic, SMX was selected as the probe to test the PMS activation performance of NMC-50 (Fig. 3(b)). Only PMS itself could degrade contaminants, the removal rates of ABEE and SMX were 50.8% and 47.5%, respectively. This indicates that PMS showed no obvious selectively for oxidation of ABEE and SMX. After the introduction of NMC-50, the degradation performance of SMX increased to 87.37%. The degradation rates of the two probes followed the order ABEE ($k_{obs} = 0.087 \, min^{-1}$) > SMX ($k_{obs} = 0.045 \, min^{-1}$). This difference was probably due to the different affinities of the substrates to the NMC-50 surface, as confirmed in Fig. S5. The surface adsorption capacity of NMC-50 for ABEE (18.85%) was higher than that for SMX (7.85%). Furthermore, the reaction rate constant between the probe and •OH/SO$_4^{\bullet-}$ might also be an important factor [42]. The profile of [PMS] was shown in Fig. S6. The oxidation of probe consumed PMS slightly. The rapid decomposition of PMS was observed at the presence of NMC-50, leading to the formation of ROS. The trend of [PMS] was consistent with the degradation of ABEE and SMX. The TOC removal efficiencies of ABEE and SMX were 35.5% or 27.7% (Fig. S7), respectively, which suggested that most ABEE and SMX molecules were probably transformed into other intermediates rather than being completely oxidized to CO$_2$ and H$_2$O.

Intermediates of ABEE or SMX from NMC-50 activation of PMS were identified by liquid chromatography–quadrupole time-of-flight mass spectrometry (LC-Q-TOF-MS). Eighteen intermediates were identified in ABEE degradation (Table S3 and Fig. S8), from which a degradation pathway for ABEE was proposed for the first time in the AOP field, as shown in Fig. 3(c). SO$_4^{\bullet-}$ is known to participate in reactions *via* electron transfer [43], with •OH attack probably occurring through electrophilic addition or hydrogen abstraction reactions [44]. Herein, a

HO$_3$SO– substitution pathway initiated by SO$_4^{\bullet-}$ was observed in ABEE degradation through PMS activation by NMC-50, with the intermediate identified as P-1. P-1 led to P-2 and P-3 through hydrogenation and oxidation reactions, respectively. Furthermore, ABEE was directly attacked by SO$_4^{\bullet-}$, resulting in -NH$_2$ group being replaced by -OSO$_3$H group to form P-6. Products of SO$_4^{\bullet-}$ attacking were unstable and undergo hydrolysis to form hydroxyl derivatives (such as P-4, P-5, and P-7). Intermediate P-12 was detected, implying that •OH attacked the benzene ring of ABEE. The -NH$_2$ group in P-12 was then oxidized to give nitro derivatives P-13 and P-14. The ester group on the benzene ring of ABEE was then oxidized to the corresponding aldehyde (P-8) and carboxylic acid (P-9), and the -NH$_2$ group in P-9 was oxidized to an -NO$_2$ group (P-10). ABEE undergoes a hydroxyl substitution reaction followed by diazotization of the -NH$_2$ group to form P-17, which then undergone further oxidation to form P-18 or hydroxyl substitution to form dihydroxy product P-16.

A SMX degradation pathway (Fig. 3(d)) was also proposed according to the identified intermediates (Table S4 and Fig. S9), among which six are reported in AOPs for the first time, as highlighted in blue. The intermediates from cleavage and oxidation by reactive species (•OH, SO$_4^{\bullet-}$, and ^{1}O$_2$) in PMS activation were identified. An important reaction pathway of SO$_4^{\bullet-}$ was initiated by electrophilic attack at the olefinic double bond in the isoxazole ring to generate an olefinic radical [45] and form PA-1 and PA-2. The amine group in the benzene ring was oxidized to a nitro group in PB-1 and PB-2, after which the hydroxyl substitution on the heterocycle formed PB-3, which was then further oxidized and undergone ring-opening to form PB-4. Direct hydroxyl substitution on the aromatic moiety of SMX was observed, with the resulting OH-SMX (PC-1) identified. Substitution of the hydroxyl group on the benzene ring of SMX by an NH$_2$ group forms PC-2 and PC-3. The S–N bond of PC-3 was likely to undergo δ-cleavage to give PC-4–PC-6 [46]. A SMX dimer was identified (PD-1) in this study, indicating a coupling reaction of aniline radicals. Then, the hydroxylation at the benzene ring was observed to form PD-2. Subsequently, electrophilic attack of •OH on the preferred sites of cleavage (N-R bond) [47] of PD-2 molecule to produce PD-3. Finally, the azo bond of PD-3 breaks to form SMX and PE-3. Furthermore, the methyl group on the isoxazole ring was oxidized to form PE-1, and then the isoxazole ring bond was cleaved to form PE-2. S–N bond cleavage then formed PE-3. The -NH$_2$ group was oxidized to a nitro group (PE-4). Finally, the ring was opened by •OH and SO$_4^{\bullet-}$ attacking, and all organic intermediates identified in this study would be further mineralized to CO$_2$ and H$_2$O *via* PMS activation by NMC-50. Being different from previous study, an initial SO$_4^{\bullet-}$ oxidation pathway was identified by the detection of PA-1 with -OSO$_3$H group.

3.4. Stability of NMC-50 in PMS activation

Ten consecutive runs of ABEE degradation were completed using NMC-50 for PMS activation (Fig. 4(a)). The performance of NMC-50 gradually decreased with each run, which might be due to active sites being blocked by ABEE degradation intermediates or iron leaching. However, as the cycling time increased, the efficiency remained unchanged, achieving about 58% removal in 60 min, indicating that the NMC-50 could be reused to activate PMS for refractory organics degradation. Compared with other Fe-based MOFs or carbon-based materials derived from Fe-based MOFs, NMC-50 shows a remarkable improvement for degradation of organic pollutant and exhibited good reusability for water treatment applications (Table S5).

Iron ion leaching might be the major reason for the decreased performance of NMC-50. Leached [Fe^{2+}] and [Fe^{3+}] were 0.19 and 1.89 mg/L after NMC-50 was used, respectively (Fig. S10 (a)). The percentage of dissolved total ions to iron content in NMC-50 is 12.3%. NMC-50 with combined addition of nitrogen sources (g-C$_3$N$_4$ and NH$_2$ groups) effectively reduced ion dissolution, compared with reported Fe@porous carbon, Fe@N-doped porous carbon [30] and Fe$_x$Co$_y$
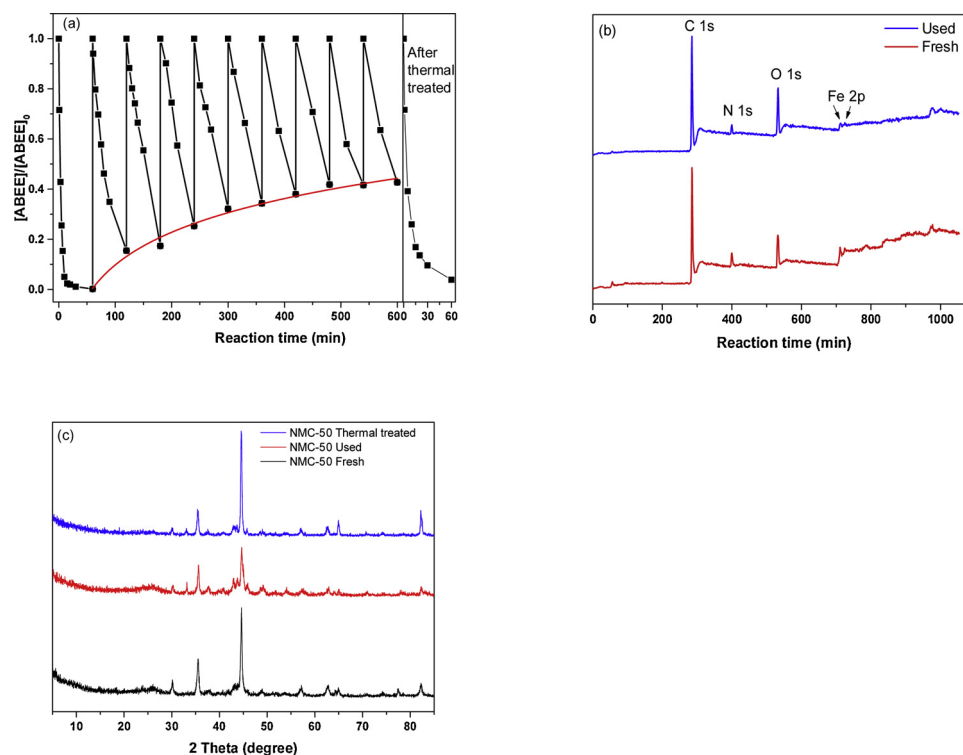
Fig. 4. The reusability of NMC-50 catalyst (a). XPS spectra of fresh and used NMC-50 (b) and XRD patterns of fresh, used and thermal treated NMC-50 (c).

nanocages [24] (Table S5). Lower ion dissolution could prolong the using life of NMC-50. However, no PMS activation performance was observed using leached iron ions (Fig. S10 (b)), indicating that iron ions leached from NMC-50 did not contribute to PMS activation for ABEE degradation. Therefore, the leached iron ions were concluded to cause the reduced performance with reuse, but NMC-50 activation of PMS was purely a heterogeneous activation.

The variation of surface morphologies was used to confirm the reason of reduced efficiency of NMC-50. Fig. S11 shows the TEM images of NMC-50 fresh and used, the framework structure of NMC-50 remains unchanged after the reaction. This was good for maintaining the higher activity of NMC-50 and confirmed the addition of g-C$_3$N$_4$ stabilized the framework structure. Additionally, the obvious aggregation of iron nanoparticles dispersed outside the framework was found, this may be another reason for the performance decreasing of the used NMC-50.

In the wide scan spectra of fresh and used NMC-50 (Fig. 4(b)), the C 1s peak basically was unchanged, while the N 1s and Fe 2p peaks became weaker. This indicated that both nitrogen and iron were lost during PMS activation by NMC-50. This was a reason for the decrease in performance with reuse. The O 1s peak became stronger after use, which might be due to the surface adsorption of intermediates containing oxygen groups on NMC-50 [21].

NMC-50 after cycling test was calcined in N$_2$ at 650°C for 1 h for reuse. 96.15% ABEE was removed within 60 min (Fig. 4(a)), which was similar with a fresh NMC-50. As shown in Fig. 4(c), XRD pattern of the used catalyst showed no obvious differences with that of the fresh catalyst, only the strength of diffraction peaks slightly weakened. However, the sample regenerated by the thermal treatment showed similar intensity of diffraction peaks as that of the fresh sample. After a thermal treatment, the adsorbed intermediates attached on the surface of NMC-50 were removed and the activity of NMC-50 was recovered. According to the regeneration result, the limited step for the performance declination was the surface of NMC-50 adsorbed intermediates formed from probe. Furthermore, to verify the adsorbed intermediates on the surface of NMC-50, we used methanol to wash the surface adsorbed intermediates, and the obtained sample was analyzed by LC-Q-

TOF-MS. The results showed that ABEE and other eight degradation products were adsorbed on the surface of the NMC-50 (Table S3), compounds with amino groups are more easily adsorbed, and this may be due to the fact that the compound readily forms hydrogen bonds with the surface of NMC-50. It indicates that the formed intermediates blocking the surface active sites led to the performance degradation of NMC-50 in the recycling process, which also indicated that this surface blocking by intermediates showed important role on performance decreasing, than other reasons.

3.5. Identification of NMC-50 reactive species for PMS activation

In previous studies, •OH and SO$_4$•$^-$ were found to be produced through PMS activation by metal-based catalysts [48] and N-doped carbon materials [49]. As shown in Fig. 5(a), negligible radicals were generated by PMS itself, while DMPO–OH (with hyperfine couplings of $\alpha_N = \alpha_{\beta-H} = 14.9$ G) [50,51] and DMPO–SO$_4$ (with hyperfine splitting constants of $\alpha_N = 13.2$ G, $\alpha_{\beta-H} = 9.6$ G, $\alpha_{\gamma-H1} = 1.48$ G, and $\alpha_{\gamma-H2} = 0.78$ G) [52,53] peaks were clearly observed in PMS activation by NMC-50. Both DMPO–OH and DMPO–SO$_4$ adducts gave highest peak intensities at about 10 min, after which the DMPO–OH intensity gradually decreased, indicating continuous •OH consumption. However, DMPO–SO$_4$ intensity showed almost no change after 10 min, implying that SO$_4$•$^-$ was consistently produced during the reaction. Furthermore, the solution pH decreased gradually as the reaction proceeded (Fig. S4), and conversion of SO$_4$•$^-$ to •OH decreased (Eq. (1)). This also led to the DMPO–OH intensity becoming weaker.

Superoxide radical anions (O$_2$•$^-$) are another ROS possibly formed during SR-AOPs [54]. As shown in Fig. 5(b), characteristic signals of DMPO–O$_2$ adduct (with hyperfine splitting constants of $\alpha_N = 14.3$ G, $\alpha_{H1} = 11.2$ G, and $\alpha_{H2} = 1.3$ G) [55] were observed in the ethanol solution. Peak intensities remained nearly constant as the reaction time was increased from 5 to 20 min, indicating that O$_2$•$^-$ were generated continuously through PMS activation by NMC-50. Interestingly, DMPO-SO$_4$ signal was also observed in ethanol. This might be due to that ethanol fails to capture surface-adsorbed radicals completely [36],
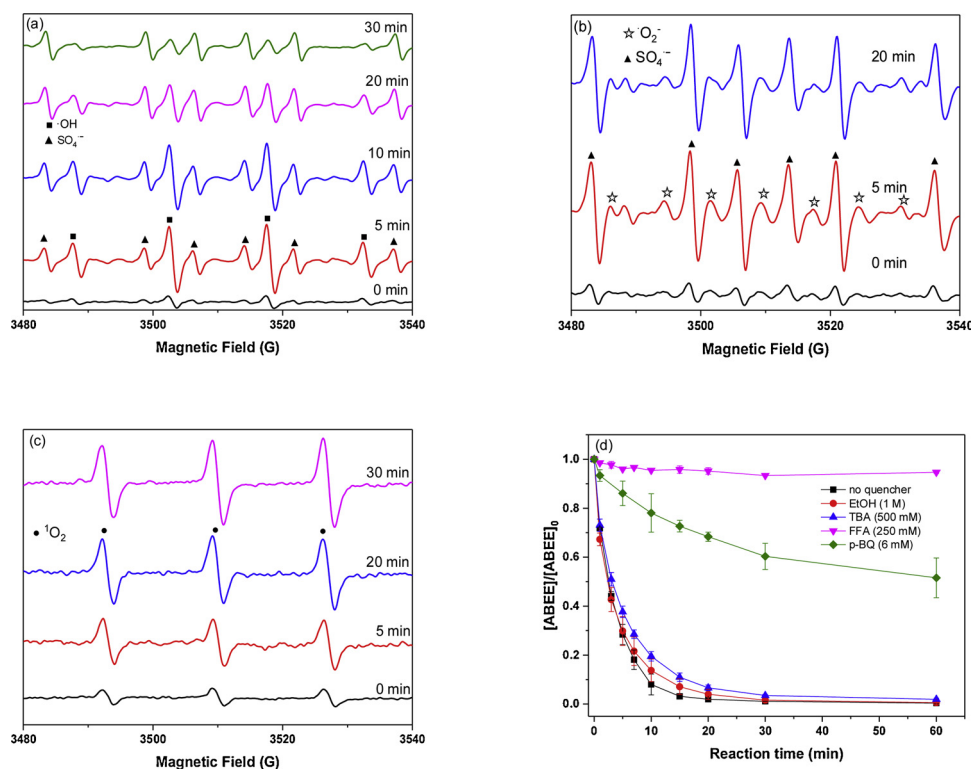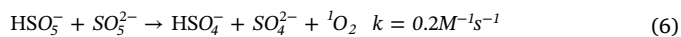
Fig. 5. EPR spectra obtained using DMPO (a), (b) and TEMP (c) as spin-trapping agents; Effects of different scavengers on the ABEE removal by NMC-50 activate PMS (d). Reaction conditions: [ABEE] = 0.06 mM, [PMS] = 0.65 mM, [NMC-50] = 50 mg/L, initial pH = 7.0.

suggesting that $SO_4^{\cdot-}$ was generated on the NMC-50 surface through PMS activation.

$^1O_2$ has also been reported to be generated by PMS self-decomposition, with a rate constant of about 0.2 $M^{-1}s^{-1}$ (Eq. (6)) [56,57].
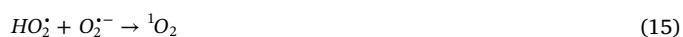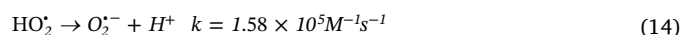
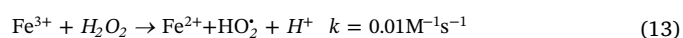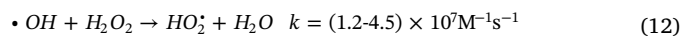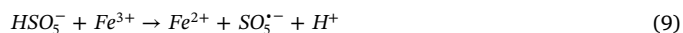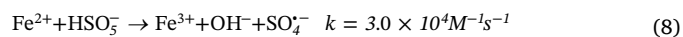$$HSO_5^- + SO_5^{2-} \rightarrow HSO_4^- + SO_4^{2-} + {}^1O_2 \quad k = 0.2 M^{-1}s^{-1} \tag{6}$$

Furthermore, $^1O_2$ has recently been reported as a dominant ROS from PMS activation by carbonaceous materials [34,58] and also been reported to preferentially oxidize electron-rich organics, such as phenols and anilines, due to its electrophilic nature [59]. Herein, when only PMS was used in solution, weak TEMPO peaks were observed due to PMS self-decomposition (Eq. (6)), as shown in Fig. 5(c). The $^1O_2$ intensity increased with NMC-50 addition, indicating that $^1O_2$ formation was increased, which is consistent with other carbonaceous materials [60]. The formation of more $^1O_2$ improved the performance of Fe@N-doped graphene-like carbon.

Quenching tests were also conducted to determine the effect of formed ROS, as shown in Fig. 5(d) and Text S6. This showed that both nonradical ($^1O_2$) and radical ($SO_4^{\cdot-}$, $O_2^{\cdot-}$, and •OH) processes were involved in ABEE degradation through PMS activation by NMC-50.

3.6. Identification of surface-active sites and derived reaction mechanism

Firstly, to confirm the contributions of iron nanoparticles and nitrogen-doped graphite-like materials to PMS activation, NMC-50 was washed with 1.0 M H_2SO_4 at 80 °C overnight to remove metallic Fe species, as used in previous reports [34,61,62]. As shown in Fig. S12, iron species were not completely removed from NMC-50 after being washed by acid solution, probably due to strong capsulation of iron species by porous carbon [22]. However, the residual iron content was too low to show any activity for PMS activation [22]. After washing, the k_{obs} value decreased from 0.078 min^{-1} to 0.068 min^{-1} (Fig. 6(a)), indicating that iron nanoparticles in NMC-50 made a weak contribution to PMS activation, compared with that of the nitrogen-doped graphite-

like material. This weak reaction might be due to the formation of •OH and $SO_4^{\cdot-}$, which were involved in electron transfer between Fe^0 and PMS, as shown in Eqs. (7)–(9) and Eq. (1). Furthermore, $O_2^{\cdot-}$ and $^1O_2$ identified by EPR might be formed, as shown in Eqs. (10)–(15). Although Fe^0 could activate PMS to generate ROS, carbon-layer-encapsulated Fe nanoparticles would prevent rapid iron corrosion and PMS preferred contact with the carbon layer. This led to Fe nanoparticles in NMC-50 showing a weak contribution to PMS activation.

$$2HSO_5^- + Fe^0 \rightarrow Fe^{2+} + 2SO_4^{\cdot-} + 2OH^- \tag{7}$$

$$Fe^{2+} + HSO_5^- \rightarrow Fe^{3+} + OH^- + SO_4^{\cdot-} \quad k = 3.0 \times 10^4 M^{-1}s^{-1} \tag{8}$$

$$HSO_5^- + Fe^{3+} \rightarrow Fe^{2+} + SO_5^{\cdot-} + H^+ \tag{9}$$

$$Fe^0 + O_2 + 2H^+ \rightarrow Fe^{2+} + H_2O_2 \tag{10}$$

$$Fe^{2+} + H_2O_2 \rightarrow Fe^{3+} + OH^- + \bullet OH \quad k = 76 M^{-1}s^{-1} \tag{11}$$

$$\bullet OH + H_2O_2 \rightarrow HO_2^\bullet + H_2O \quad k = (1.2\text{-}4.5) \times 10^7 M^{-1}s^{-1} \tag{12}$$

$$Fe^{3+} + H_2O_2 \rightarrow Fe^{2+} + HO_2^\bullet + H^+ \quad k = 0.01 M^{-1}s^{-1} \tag{13}$$

$$HO_2^\bullet \rightarrow O_2^{\cdot-} + H^+ \quad k = 1.58 \times 10^5 M^{-1}s^{-1} \tag{14}$$

$$HO_2^\bullet + O_2^{\cdot-} \rightarrow {}^1O_2 \tag{15}$$

High-resolution Fe spectra (Fig. S13(a)) showed that Fe^0, Fe^{3+}, Fe^{2+} and shake-up satellite Fe $2p_{3/2}$ were present on NMC-50 surface. After use, Fe^0 peak was slightly reduced (Fig. S13(b)) and the ratio of Fe^{2+}/Fe^{3+} was increased from 1.28 to 1.42. This result indicated that Fe^0 in NMC-50 was oxidized to Fe^{2+} by PMS and formed ROS (Eqs. (7) and (8)), and Fe^{3+} might react with PMS to produce $SO_5^{\cdot-}$ and Fe^{2+} (Eq. (9)). Furthermore, Fe^{3+} could be reduced to Fe^{2+} by Fe^0 (Eq. (16)). Therefore, the proportion of Fe^{3+} decreased after PMS activation. The deconvolution of O 1s, N 1s, and C 1s in fresh and used NMC-50 is shown in Figs. S13 and S14, and Text S7.
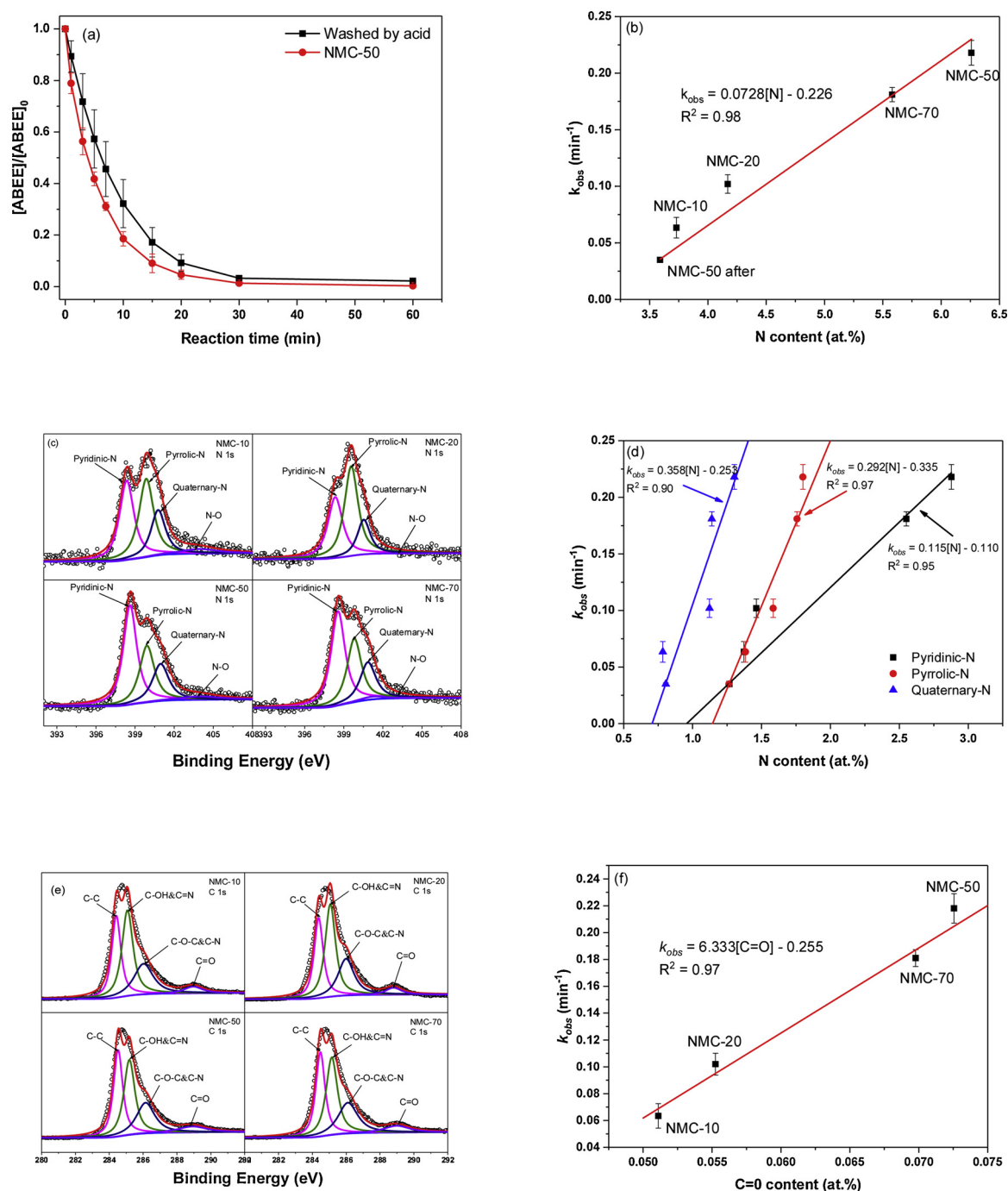
Fig. 6. Removal efficiency of ABEE by NMC-50 and acid-treated NMC-50 activated PMS (a); Effect of N content on the degradation efficiency of ABEE (b); XPS high-resolution spectrum of N1s (c); Effect of N content of different nitrogen species on the degradation efficiency of ABEE (d); XPS high-resolution spectrum of C 1s (e); Effect of C=O content of carbon on the degradation efficiency of ABEE (f).

$$Fe^0 + 2Fe^{3+} \rightarrow 3Fe^{2+} \tag{16}$$

Fig. 6(b) shows that k_{obs} was enhanced with increasing nitrogen content, suggesting that the nitrogen group in Fe@N-doped graphene-like carbon structure played a positive role in PMS activation. In addition to the nitrogen doping mass, the nitrogen species also influenced the catalytic activity [63,64]. Nitrogen XPS analysis before and after the reaction (Text S7) was used to determine the involvement of nitrogen in PMS activation. The N 1s spectrum could be deconvoluted into four components, namely, pyridinic-N (398.6 eV), pyrrolic-N (399.6 eV), quaternary-N (401.1 eV), and N–O (403.9 eV) (Fig. 6(c)). The content of each nitrogen species in the sample changed with increasing g-C$_3$N$_4$

addition. As shown in Fig. 6(d), pyridinic-N, pyrrolic-N, and quaternary-N were favorable for improving k_{obs}. As higher slope values indicated a more significant positive contribution to the enhanced performance, the contributions of the nitrogen species were in the order quaternary-N > pyrrolic-N > pyridinic-N.

It has been reported that sp^2-C and electron-rich oxides, including C–O and C=O groups, might act as interface active sites for PMS activation [65]. Four peaks were deconvoluted into C–C (284.7 eV), C=N (284.9 eV), C–N (286.2 eV), and C=O (288.6 eV) components (Fig. 6(e)). However, only C=O was favorable for improving k_{obs} with increasing g-C$_3$N$_4$ content (Fig. 6(f)). C=O groups play a vital role in interacting with PMS through nucleophilic addition and mediating a
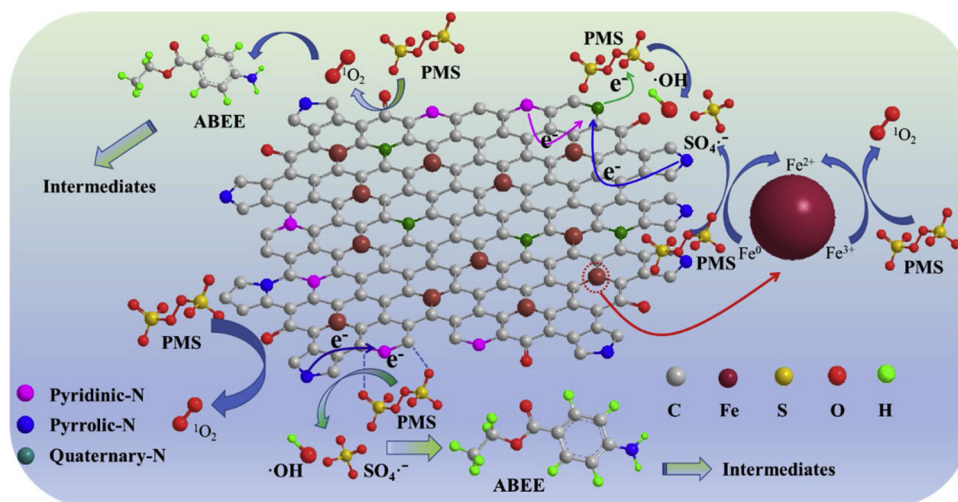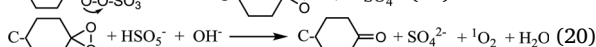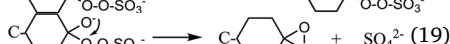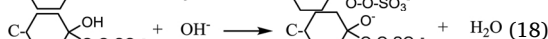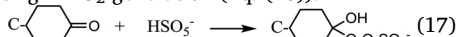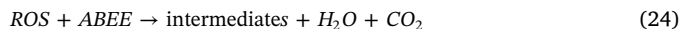
Fig. 7. Schematic illustration of the reaction mechanism for ABEE removal by NMC-50 activated PMS.

peroxide intermediate for $^1O_2$ evolution, as identified by EPR (Fig. 5(c)) [16]. C=O groups at the boundaries of sp^2-conjugated carbon lattices might be active sites for $^1O_2$ evolution.

According to above results, quaternary-N, pyrrolic-N, pyridinic-N, and C=O groups were identified as active sites for ROS evolution. A possible mechanism for PMS activation by NMC-50 for ABEE degradation is shown in Fig. 7. (i) sp^2-hybridized carbon, proven to be an excellent electron-transfer support [66], activated PMS *via* electron transfer to generate $SO_4^{\bullet-}$ and •OH radicals. C=O groups in the NMC-50 structure, were shown to be functional groups for PMS activation, in agreement with another report [16]. HSO_5^- species attacked the C=O group of NMC-50 to form peroxide adducts (Eq. (17)). After deprotonation in the presence of hydroxide ions (Eq. (18)), the adduct decomposed to a dioxirane intermediate and SO_4^{2-} through intramolecular nucleophilic displacement of the alkoxide oxygen at the O–O bond (Eq. (19)). HSO_5^- then attacked the dioxirane adduct, resulting in $^1O_2$ generation (Eq. (20)).

$$C\text{-}\!\!\!\!=\!\!O + HSO_5^- \longrightarrow C\text{-}\overset{OH}{\underset{O\text{-}O\text{-}SO_3^-}{\big\langle}} \quad (17)$$

$$C\text{-}\overset{OH}{\underset{O\text{-}O\text{-}SO_3^-}{\big\langle}} + OH^- \longrightarrow C\text{-}\overset{O^-}{\underset{O\text{-}O\text{-}SO_3^-}{\big\langle}} + H_2O \quad (18)$$

$$C\text{-}\overset{O^-}{\underset{O\text{-}O\text{-}SO_3^-}{\big\langle}} \longrightarrow C\text{-}\overset{O}{\underset{O}{\big\langle}} + SO_4^{2-} \quad (19)$$

$$C\text{-}\overset{O}{\underset{O}{\big\langle}} + HSO_5^- + OH^- \longrightarrow C\text{-}\!\!\!=\!\!O + SO_4^{2-} + {}^1O_2 + H_2O \quad (20)$$

(ii) as previously reported, doped N induced electron transfer from adjacent carbon to nitrogen, leading to formation of electron-rich sp^2 sites in the graphitic domain [67]. In this process, PMS first attached in close proximity to the surface of N-doped carbon layer [68], and then the peroxide bond (O–O) of PMS was cleaved by accepting one electron from NMC-50 to generate $SO_4^{\bullet-}$ and •OH (Eqs. (21) and (1)). Theoretical calculations also demonstrated that quaternary N showed a strong adsorption ability for PMS compared with pyridinic-N and pyrrolic-N [69], in agreement with this study. Therefore, quaternary N might first chemically adsorbed HSO_5^- and then donated one electron to break the O–O bond (HO–SO_4^-) and complete PMS activation [69]. Furthermore, pyridinic and pyrrolic N, as Lewis basic sites bearing lone electron pairs, was able to transfer electrons to activate PMS and generate radicals (Eq. (21) [70]). Subsequently, $SO_4^{\bullet-}$ and •OH were translated into $^1O_2$ and $O_2^{\bullet-}$ (Eqs. (22),(23), and (12)-(15)). Finally, refractory organics were oxidized by the formed ROS and decompose to CO_2 and H_2O (Eq. (24)).

$$HSO_5^- + e^- \rightarrow SO_4^{\bullet-} + OH^- \quad (21)$$

$$HSO_5^- + H_2O \rightarrow H_2O_2 + HSO_4^- \quad (22)$$

$$H_2O_2 \rightarrow H^+ + HO_2^{\bullet} \quad (23)$$

$$ROS + ABEE \rightarrow intermediates + H_2O + CO_2 \quad (24)$$

4. Conclusions

A facile route has been developed for the fabrication of a novel PMS activation mediator (Fe@N-doped graphene-like carbon) by direct pyrolysis of a combination of g-C_3N_4 and NH_2-MIL-53(Fe) under N_2. The addition of combined nitrogen sources not only improved the stability of the phase composition and framework morphology in the final products, but also significantly improved PMS activation performance. The presence of •OH, $SO_4^{\bullet-}$, $O_2^{\bullet-}$, and $^1O_2$ was identified, with a combination of nonradical and radical oxidation processes accounting for organics degradation. Iron nanoparticles in NMC-50 played a weak role in PMS activation, but contributed to the magnetic separation of NMC-50 from aqueous media. Quaternary-N, pyrrolic-N, pyridinic-N, and C=O groups on the surface of Fe@N-doped graphene-like carbon were identified as active sites for PMS activation. This study provided a new insight to fabricate high efficiency activation mediator combined metal and N-doped graphene-like carbon from MOFs for advanced oxidation processes.

Appendix A. Supplementary data

Supplementary material related to this article can be found, in the online version, at doi:https://doi.org/10.1016/j.apcatb.2019.117763.

References

[1] W.-D. Oh, V.W.C. Chang, Z.-T. Hu, R. Goei, T.-T. Lim, Chem. Eng. J. 323 (2017) 260–269.
[2] J. Chen, H. Luo, H. Shi, G. Li, T. An, Appl. Catal. A Gen. 485 (2014) 188–195.
[3] P. Hu, M. Long, X. Bai, C. Wang, C. Cai, J. Fu, B. Zhou, Y. Zhou, J. Hazard. Mater. 332 (2017) 195–204.
[4] H. Gao, H. Yang, J. Xu, S. Zhang, J. Li, Small 14 (2018) 1801353.
[5] R. Luo, C. Liu, J. Li, J. Wang, X. Hu, X. Sun, J. Shen, W. Han, L. Wang, J. Hazard. Mater. 329 (2017) 92–101.
[6] F. Ghanbari, M. Moradi, Chem. Eng. J. 310 (2017) 41–62.
[7] Y.H. Guan, J. Ma, X.C. Li, J.Y. Fang, L.W. Chen, Environ. Sci. Technol. 45 (2011) 9308–9314.

[8] R.L. Johnson, P.G. Tratnyek, R.O. Johnson, Environ. Sci. Technol. 42 (2008) 9350–9356.

[9] O.S. Furman, A.L. Teel, R.J. Watts, Environ. Sci. Technol. 44 (2010) 6423–6428.

[10] G.P. Anipsitakis, D.D. Dioysiou, Environ. Sci. Technol. 38 (2004) 3705–3712.

[11] W.-D. Oh, Z. Dong, T.-T. Lim, Appl. Catal. B 194 (2016) 169–201.

[12] S.X. Liang, Z. Jia, W.C. Zhang, X.F. Li, W.M. Wang, H.C. Lin, L.C. Zhang, Appl. Catal. B 221 (2018) 108–118.

[13] Z. Jia, X. Duan, P. Qin, W. Zhang, W. Wang, C. Yang, H. Sun, S. Wang, L.-C. Zhang, Adv. Funct. Mater. 27 (2017) 1702258.

[14] S.X. Liang, Z. Jia, Y.J. Liu, W. Zhang, W. Wang, J. Lu, L.C. Zhang, Adv. Mater. 30 (2018) 1802764.

[15] M. Rimoldi, A.J. Howarth, M.R. DeStefano, L. Lin, S. Goswami, P. Li, J.T. Hupp, O.K. Farha, ACS Catal 7 (2016) 997–1014.

[16] D. Li, X. Duan, H. Sun, J. Kang, H. Zhang, M.O. Tade, S. Wang, Carbon 115 (2017) 649–658.

[17] G. Wang, S. Chen, X. Quan, H. Yu, Y. Zhang, Carbon 115 (2017) 730–739.

[18] Y. Gong, X. Zhao, H. Zhang, B. Yang, K. Xiao, T. Guo, J. Zhang, H. Shao, Y. Wang, G. Yu, Appl. Catal. B 233 (2018) 35–45.

[19] K.-Y. Andrew Lin, F.-K. Hsu, W.-D. Lee, J. Mater. Chem. A 3 (2015) 9480–9490.

[20] H.D. Mai, K. Rafiq, H. Yoo, Chemistry 23 (2017) 5631–5651.

[21] T. Zeng, M. Yu, H. Zhang, Z. He, J. Chen, S. Song, Catal. Sci. Technol. 7 (2017) 396–404.

[22] P. Liang, C. Zhang, X. Duan, H. Sun, S. Liu, O.T. Moses, S. Wang, ACS Sustain. Chem. Eng. 5 (2017) 2693–2701.

[23] K.Y. Lin, B.C. Chen, Dalton Trans 45 (2016) 3541–3551.

[24] X. Li, A.I. Rykov, B. Zhang, Y. Zhang, J. Wang, Catal. Sci. Technol. 6 (2016) 7486–7494.

[25] W. Gu, L. Hu, J. Li, E. Wang, ACS Appl. Mater. Interfaces 8 (2016) 35281–35288.

[26] S. Zhang, H. Gao, Y. Huang, X. Wang, T. Hayat, J. Li, X. Xu, X. Wang, Environ. Sci.: Nano 5 (2018) 1179–1190.

[27] X. Wang, K. Maeda, A. Thomas, K. Takanabe, G. Xin, J.M. Carlsson, K. Domen, M. Antonietti, Nat. Mater 8 (2008) 76–80.

[28] A.J. Li, Z. Sang, C.H. Chow, J.C. Law, Y. Guo, K.S. Leung, J. Hazard. Mater. 337 (2017) 115–125.

[29] D.W. Kolpin, E.T. Furlong, M.T. Meyer, E.M. Thurman, S.D. Zaugg, L.B. Barber, H.T. Buxton, Environ. Sci. Technol. 36 (2002) 1202–1211.

[30] C. Liu, Y. Wang, Y. Zhang, R. Li, W. Meng, Z. Song, F. Qi, B. Xu, W. Chu, D. Yuan, B. Yu, Chem. Eng. J 354 (2018) 835–848.

[31] E.T. Yun, J.H. Lee, J. Kim, H.D. Park, J. Lee, Environ. Sci. Technol. 52 (2018) 7032–7042.

[32] Y. Feng, C. Liao, L. Kong, D. Wu, Y. Liu, P.H. Lee, K. Shih, J. Hazard. Mater. 354 (2018) 63–71.

[33] H. Dong, M. Wei, J. Li, J. Fang, L. Gao, X. Li, A. Xu, RSC Adv. 6 (2016) 70747–70755.

[34] P. Liang, C. Zhang, X. Duan, H. Sun, S. Liu, M.O. Tade, S. Wang, Environ. Sci.: Nano 4 (2017) 315–324.

[35] M. Wei, L. Gao, J. Li, J. Fang, W. Cai, X. Li, A. Xu, J. Hazard. Mater. 316 (2016) 60–68.

[36] Y. Lei, C.S. Chen, Y.J. Tu, Y.H. Huang, H. Zhang, Environ. Sci. Technol. 49 (2015) 6838–6845.

[37] T. Zhang, H. Zhu, J.-P. Croué, Environ. Sci. Technol. 47 (2013) 2784–2791.

[38] M. Zhang, C. Wang, C. Liu, R. Luo, J. Li, X. Sun, J. Shen, W. Han, L. Wang, J. Mater. Chem. A 6 (2018) 11226–11235.

[39] G.V. Buxton, C.L. Greenstock, W.P. Helman, A.B. Ross, J. Phys. Chem. Ref. Data 17 (1988) 513–886.

[40] Y. Wang, C. Liu, Y. Zhang, W. Meng, B. Yu, S. Pu, D. Yuan, F. Qi, B. Xu, W. Chu, Appl. Catal. B 235 (2018) 264–273.

[41] R. Yuan, L. Hu, P. Yu, H. Wang, Z. Wang, J. Fang, Chemosphere 198 (2018) 204–215.

[42] Y. Ding, W. Nie, W. Li, Q. Chang, Chem. Eng. J. 356 (2019) 359–370.

[43] P. Neta, V. Madhavan, H. Zemel, R.W. Fessenden, J. Am. Chem. Soc. 99 (1977) 163–164.

[44] C. Cai, Z. Zhang, H. Zhang, J. Hazard. Mater. 313 (2016) 209–218.

[45] Y. Wang, X. Lu, J. Jiang, J. Ma, G. Liu, Y. Cao, W. Liu, J. Li, S. Pang, X. Kong, C. Luo, Water Res. 118 (2017) 196–207.

[46] Y. Ji, Y. Fan, K. Liu, D. Kong, J. Lu, Water Res. 87 (2015) 1–9.

[47] K.P. de Amorim, L.L. Romualdo, L.S. Andrade, Sep. Purif. Technol. 120 (2013) 319–327.

[48] W. Wang, H. Sun, X. Duan, H.M. Ang, M.O. Tadé, S. Wang, Appl. Catal. B 172-173 (2015) 73–81.

[49] S. Indrawirawan, H. Sun, X. Duan, S. Wang, J. Mater. Chem. A 3 (2015) 3432–3440.

[50] Y. Wang, Z. Ao, H. Sun, X. Duan, S. Wang, Appl. Catal. B 198 (2016) 295–302.

[51] H. Gao, R. Cao, X. Xu, S. Zhang, H. Yongshun, H. Yang, X. Deng, J. Li, Appl. Catal. B 245 (2019) 399–409.

[52] G.X. Huang, C.Y. Wang, C.W. Yang, P.C. Guo, H.Q. Yu, Environ. Sci. Technol. 51 (2017) 12611–12618.

[53] P.L. Zamora, F.A. Villamena, J. Phys. Chem. A 116 (2012) 7210–7218.

[54] C. Qi, X. Liu, J. Ma, C. Lin, X. Li, H. Zhang, Chemosphere 151 (2016) 280–288.

[55] W. Qin, G. Fang, Y. Wang, D. Zhou, Chem. Eng. J. 348 (2018) 526–534.

[56] D.F. Evans, M.W. Upton, J. Chem. Soc., Dalton Trans. 6 (1985) 1151.

[57] D.L. Ball, John O. Edwards, J. Am. Chem. Soc. 78 (1956) 1125–1129.

[58] Z. Zhu, C. Ji, L. Zhong, S. Liu, F. Cui, H. Sun, W. Wang, J. Mater. Chem. A 5 (2017) 18071–18080.

[59] M. Jiang, Q. Zhang, Y. Ji, D. Kong, J. Lu, X. Yin, Q. Zhou, C. Ferronato, J.M. Chovelon, Sci. Total. Environ. 636 (2018) 864–871.

[60] J. Hou, S. Yang, H. Wan, H. Fu, X. Qu, Z. Xu, S. Zheng, Chemosphere 197 (2018) 485–493.

[61] Y. Liu, H. Wang, D. Lin, J. Zhao, C. Liu, J. Xie, Y. Cui, Nano Res. 10 (2017) 1213–1222.

[62] N. Wang, W. Ma, Z. Ren, L. Zhang, R. Qiang, K.-Y.A. Lin, P. Xu, Y. Du, X. Han, Inorg. Chem. Front. 5 (2018) 1849–1860.

[63] X. Duan, Z. Ao, H. Sun, L. Zhou, G. Wang, S. Wang, Chem. Commun. 51 (2015) 15249–15252.

[64] H.W. Liang, X. Zhuang, S. Bruller, X. Feng, K. Mullen, Nat. Commun. 5 (2014) 4973.

[65] W. Peng, H. Sun, Y. Yao, L. Zhic, S. Wang, J. Mater. Chem. A 1 (2013) 5854–5859.

[66] M. Feng, R. Qu, X. Zhang, P. Sun, Y. Sui, L. Wang, Z. Wang, Water Res. 85 (2015) 1–10.

[67] X. Chen, W.-D. Oh, Z.-T. Hu, Y.-M. Sun, R.D. Webster, S.-Z. Li, T.-T. Lim, Appl. Catal. B 225 (2018) 243–257.

[68] N. Wang, W. Ma, Z. Ren, Y. Du, P. Xu, X. Han, J. Mater. Chem. A 6 (2018) 884–895.

[69] X. Duan, Z. Ao, H. Sun, S. Indrawirawan, Y. Wang, J. Kang, F. Liang, Z.H. Zhu, S. Wang, ACS Appl. Mater. Interfaces 7 (2015) 4169–4178.

[70] B. Frank, J. Zhang, R. Blume, R. Schlogl, D.S. Su, Angew. Chem. Int. Ed, Engl. 48 (2009) 6913–6917.